


REVIEW

Schlieren techniques for observations of long positive sparks: Review and application

Junjia He¹ | Xiankang Wang¹  | Xiangen Zhao^{1,2}  | Juhyeong Lee³ |
Yaping Du² | Xiaopeng Liu¹ | Quan Gan¹ | Yang Liu¹ | Yuqin Liao¹

¹State Key Laboratory of Advanced Electromagnetic Engineering and Technology, Huazhong University of Science and Technology, Wuhan, China

²Department of Building Environment and Energy Engineering, Hong Kong Polytechnic University, Kowloon, China

³Department of Mechanical and Aerospace Engineering, Utah State University, Logan, Utah, USA

Correspondence

Xiangen Zhao, Department of Building Environment and Energy Engineering, Hong Kong Polytechnic University, Kowloon, Hong Kong, China.

Email: zhaoxiangen@outlook.com

Associate Editor: Fan Yang

Funding information

China Postdoctoral Science Foundation, Grant/Award Number: 2018M633193; National Natural Science Foundation of China, Grant/Award Number: 51821005

Abstract

Understanding the mechanism of positive leader discharge is important in lightning protection engineering and the external insulation design in high voltage power transmission systems. During the propagation of a positive leader, some processes without light-emitting, for example, the insulation recovery process after the breakdown, cannot be observed by optical photography techniques. With the combination of the digital high-speed imaging system, the conventional Schlieren techniques offer new vistas in the long air gap discharge observation. The important features of high spatial resolution, high sensitivity, and easy arrangement make Schlieren techniques powerful and effective tools for characterising the discharge processes without light-emitting. This work presents a brief review of current Schlieren techniques and discusses the design of the Schlieren optics system for long spark observations. Several interesting phenomena discovered at different phases of long sparks with high-speed Schlieren techniques are also presented.

1 | INTRODUCTION

Understanding the mechanism of positive leaders is essential in high voltage engineering and lightning protection system design [1–4]. Since the 1960s, driven by the external insulation problems in the field of Extra High Voltage and Ultra High Voltage power transmission systems, the initiation and propagation features of positive and negative leader discharges have been investigated both experimentally and theoretically [5–11]. It is widely accepted that the discharge in long air gaps under positive impulse voltages involves several primary chronological sequences. Figure 1 shows the sketch of different phases, and their features are described as follows.

(a) Streamer-corona burst.

The streamer corona takes the form of several narrow-branched channels (streamers) developing from a common root called *stem* [12–14] or *leader head* [15]. The associated electric current waveform usually consists of a steep front of 5–10 ns followed by an exponential decay with a time constant of 200–500 ns [12]. With the current injected into the short, thin stem, the gas temperature inside the stem instantaneously increases from room temperature (300 K) to over 1000 K [16, 17], accompanied by observable light-emitting.

(b) Dark period.

A dark period refers to the time interval when no apparent ionizing activity can be observed, specifically, the time interval between the streamer-corona bursts before the leader initiation [18, 19]. When the electric field near the electrode is not

This is an open access article under the terms of the Creative Commons Attribution-NonCommercial-NoDerivs License, which permits use and distribution in any medium, provided the original work is properly cited, the use is non-commercial and no modifications or adaptations are made.

© 2022 The Authors. *High Voltage* published by John Wiley & Sons Ltd on behalf of The Institution of Engineering and Technology and China Electric Power Research Institute.

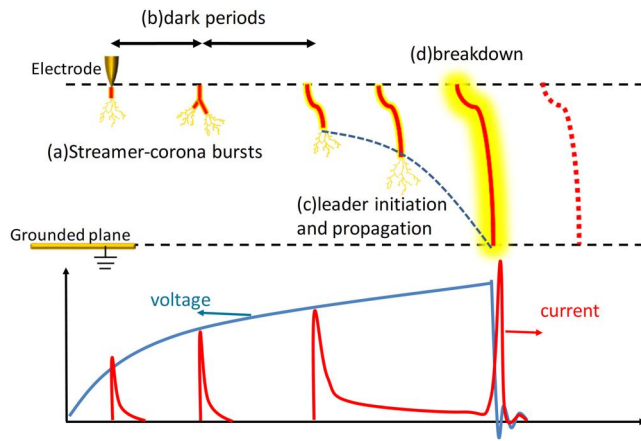


FIGURE 1 Conceptual sketch showing sequential phases of a long spark under a typical positive impulse voltage

sufficiently strong (due to either a slow rise rate of the applied impulse voltage or the inhabitation of the space charge or both) to trigger the initiation of a leader, the discharge may stop temporarily, and the dark period may occur subsequently [12]. During a dark period, the illumination is nearly indiscernible [20], and the temperature of the discharge channel decreases due to the convective heat transfer with the surrounding air [20–23]. Recently, researchers [24, 25] observed faint illumination along the residual stem channel during a dark period, but the light-emitting mechanism is unclear. For simplicity, the term dark period is typically used to indicate this process although it is not dark.

(c) Leader formation and propagation.

The electric current created by the streamers, with an amplitude of several amperes, converges to the stem, and the associated electrical energy is instantaneously dissipated as thermal energy due to Joule heating [12]. Then, the phenomenon called *thermal ionization instability* [5, 11] is triggered, and the cold streamer corona (~ 300 K) is transformed to a hot leader channel (over 5000 K) within a $1 \mu\text{s}$ time scale [11]. Sequentially, the positive leader advances towards the grounded plane with the leader corona developing in front of its head. The positive leader advancement velocity is in the order of 10^4 m/s for long sparks in the laboratory [26] or even 10^5 m/s for natural lightning [27–29].

(d) Breakdown.

The following breakdown phase is evitable when the streamer corona finally reaches the grounded plane [30]. The thin channel with high electrical conductivity bridges the high voltage (HV) electrode and the grounded plane. Accordingly, the electric current pulse with an amplitude of several thousands of amperes passes through the channel and rapidly heats the neutral air to over 10,000 K within several microseconds [31]. At such a high temperature, the leader channel is transformed into an arc channel with intensive illumination. The

high temperature, highly compressed arc channel pressurises the surrounding air and creates shock waves that propagate radically at supersonic velocity [11, 17, 32].

(e) Insulation recovery.

Once the leader aborts during propagation or finally bridges the air gap, a relaxation phase occurs in the leader channel. With the discharge activities stopping and no energy injected through the leader channel, the channel temperature decreases dramatically due to convection with the surrounding cool air, decreasing channel electrical conductivity [33–35]. The channel evolution at this phase is mainly controlled by three-dimensional Navier–Stokes equations. Comprehensive kinetic schemes should also be employed to describe the changes in plasma composition and the energy exchanges between active particles [17].

Discharge processes with light-emitting have been extensively observed and studied by using optical imaging techniques, for example, streak camera [12, 36], high-speed video camera [18, 37–39], or intensified charge-coupled device (ICCD) camera [30, 40]. However, limited studies exist on lightless phases like dark periods or insulation recovery phases during which the thermodynamics process is predominant instead of the ionization process.

Non-contact optical measurement methods are typically employed to shed new light on the thermal characteristics of the leader discharges in long air gaps. Schlieren techniques, featured with high sensitivity and moderate spatial resolution in two dimensions [41], are proven to be good choices in observing different phases in the long air gap discharges by striking a balance among sensitivity, spatial resolution, ease of use, and cost factor. Some novel phenomena in laboratory sparks have been discovered in the past few decades by combining conventional Schlieren optics and digital high-speed imaging systems.

This paper aims to provide a brief review of the Schlieren techniques and compare various Schlieren optics systems to find a better solution for the observations of long sparks (Section 2). Then, the selection of essential parameters of a Schlieren system is thoroughly discussed in Section 3. With the proposed Schlieren system configurations, numerous observations were carried out on different phases of long sparks. Some of the recent discoveries are highlighted in Section 4. In Section 5, the advantages of Schlieren techniques in long air gap discharge observations are summarised.

2 | SCHLIEREN OPTICS SYSTEMS

Fundamentally, the Schlieren optics system can detect refractive index deviation in a transparent medium [41]. Figure 2 details the configurations of a typical Toepler's lens-type Schlieren system. The conventional arrangement of a Toepler's lens-type optic starts with a point light source. A collimating lens is used to produce a collimating light beam from the point light source and project the light beam to a target

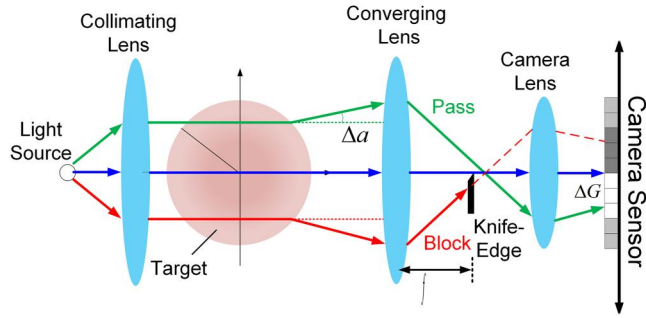


FIGURE 2 Schematic of a Toepler's lens-type Schlieren optics system

object. The light beam deflects when passing through the discharge channel with non-uniform air density distribution. Then, a deflection angle $\Delta\alpha$ is converted to the greyscale variation ΔG in the images by a knife edge located at the focus of the converging lens with a focal length f . If the light beam is deflected away from the knife edge (green path in Figure 2), more light will enter the camera, and the corresponding pixels of the image will have a larger greyscale value than the undisturbed region. Conversely, if the light beam is deflected towards the knife edge (red path in Figure 2), the corresponding part of the image will have a lower greyscale value.

The lens diameter determines the field of view (FOV) of the Toepler's lens-type Schlieren optics. To observe small targets (typically, a few cm in diameter), the Toepler's lens-type system is a good choice since it provides satisfactory image quality and straightforward arrangement [42]. The diameter of a commercial achromatic lens is no larger than 15 cm (6 inches), limiting the FOV of Toepler's lens-type Schlieren optics. If an FOV of over 15 cm is required, other Schlieren optics types should be alternatively chosen. Figure 3 shows additional three Schlieren optics with larger FOV, that is, the Z-type, the retroreflective type, and the Background-Oriented Schlieren (BOS) type.

The Z-type Schlieren optics (Figure 3a) with two parabolic mirrors is alternatively used. Using two parabolic mirrors can fold the optical path and makes Z-type Schlieren optics immune from off-axis aberration, which is inevitable in a large diameter Toepler's lens-type optics. The parabolic mirrors with diameters up to tens of centimetres are provided from commercial telescope manufacturers, making the Z-type Schlieren applied primarily in flow dynamics research [42].

To achieve a larger FOV of over 1 m, the retroreflective materials, represented by 3M™ Scotchlite™ series, are used to replace the expensive optical lens and mirrors. Figure 3b shows a typical arrangement of large FOV Schlieren with a retroreflective screen [43]. The FOV of the retroreflective system can be further expanded by splicing multiple screens. For example, researchers from the National Aeronautics and Space Administration (NASA) achieve an FOV of about 4.9 m by 4.9 m by splicing small retroreflective screens [44].

The BOS is the most significant development for Schlieren techniques in the last few decades [45–49]. In contrast to three previous Schlieren systems that require costly and fragile optics components, the BOS in Figure 3c uses a dot pattern

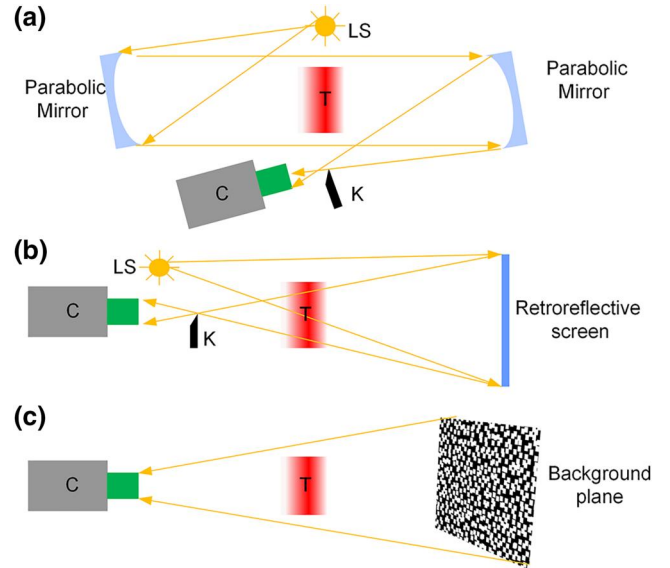


FIGURE 3 Diagrammatic sketches of other three typical types of Schlieren optics: (a) Z-type, (b) retroreflective type, and (c) Background-Oriented Schlieren (BOS) type. LS, T, K, and C indicate the light source, observation target, knife-edge, and camera, respectively. Other optic components used in specific Schlieren optics are indicated in each corresponding subfigure

background and the correlation-based image process to characterise the flow field [46]. Several image-processing algorithms [50–52] have been developed to transform displacements of the spots on the camera image sensor to the deviation angle of the light when passing through the target. The BOS system combines the advantages of a large FOV, relatively cheap (but accurate) optics, and acceptable image quality. Therefore, this system has been widely used in the fluid dynamic research since its invention in the 1990s [45]. However, one of the major disadvantages of using the BOS techniques is their limited spatial resolution compared with traditional Schlieren optics in Figures 2 and 3a [45]. The image-processing algorithms used in BOS require a larger interrogation window to improve the sensitivity, decreasing the spatial resolution, especially when the BOS is equipped with high-speed video cameras that have limited pixel density [53].

3 | DESIGN OF SCHLIEREN OPTICS SYSTEM FOR LONG SPARK OBSERVATIONS

The spatial and temporal evolutions of the discharge process are the two main factors that need to be carefully considered when designing a Schlieren system. The spatial scale of the observation target determines the required FOV and spatial resolution, and the air density gradient determines the needed sensitivity. Based on these, the type of proper Schlieren optics and the size of the light source spot can be selected. Finally, the light source with enough optical power has to be chosen. Moreover, the imaging system should be designed according to

the temporal resolution of the discharge process of interest. The evolution time of the discharge process determines the required recoding time and frame rate. The design flow chart of a Schlieren system can be referred to in Figure 4.

Determining the key parameters of a Schlieren system is complicated as many observation requirements, such as the temporal and spatial resolutions and FOV, are mutually restricted. Therefore, trial-and-error is inevitable in the process of balancing these requirements. However, according to our experience, there are still some basic principles for readers to refer to, which can help improve the design efficiency, and are detailed in the following sections.

3.1 | Design of Schlieren optics system for long spark observations

3.1.1 | Choose a proper Schlieren optics type

The selection of a proper Schlieren system strongly depends on observation targets and processes of interest. Table 1 compares several key features of four Schlieren optics systems mentioned in Section 2. For the observation of small objects, the traditional Toepler's lens-type system is recommended for its good image quality and easy arrangement feature. The Z-type system with FOV (as large as 50 cm) is preferable for objects larger than 15 cm in size. For even larger objects, for example, the discharge channel in the metre-scale air gap, the retroreflective system, and BOS system are preferred. As the discharge channel is always thin (\sim mm or \sim cm), the digital camera used in the BOS system should have a relatively high pixel density to achieve sufficient spatial resolution. Comprehensively considering the FOV, spatial resolution, and arrangement difficulties, the Toepler's lens-type Schlieren optics system in Figure 2 is recommended to observe different phases of long sparks.

3.1.2 | Optimise the sensitivity of the Schlieren system

One of the important parameters of the Schlieren optics is its sensitivity. The Schlieren optics with very high sensitivity can form a sharp image but are not suitable for the quantitative observation because a slight deflection angle may cause saturation of the greyscale value in Schlieren images. In contrast, the Schlieren system may not capture small air density changes if the sensitivity is too low. The sensitivity is determined by the focal length of the converging lens (see Figure 2). We have tried four converging lenses with 100 mm, 150 mm, 180 mm, and 200 mm lens diameters and their corresponding focal lengths of 1000 mm, 1500 mm, 1800 mm, and 2000 mm, respectively. It is shown that the latter three groups of lenses can provide proper sensitivity. Note that the lens parameters mentioned above are the best recommendation for our Schlieren system setups, and readers can select suitable lenses according to their experimental platforms. The following are three key lens selection guidelines. (1) The air gap length needs

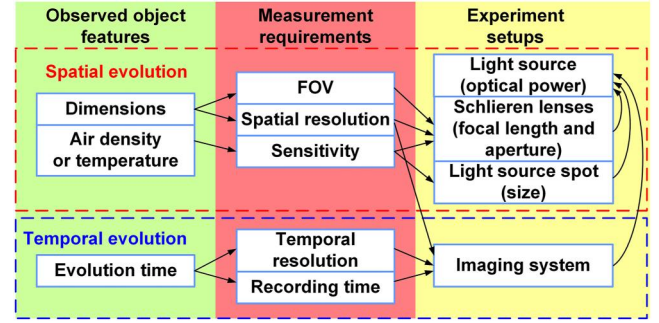


FIGURE 4 Schematic diagram of the process of determining the key parameters of a Schlieren system

to match the lens's focal length as the observed object needs to be imaged within the focal length of the converging lens. When considering the safety factor, the gap length should not exceed the focal length, especially in the case of breakdown. (2) The space of the experimental site needs to be considered if Schlieren optics with a longer focal length is chosen. (3) It is better to use the commercially available lens.

3.1.3 | Choose the light source

The light source should be optimised when the quantitative measurement of the formation and development of a spark channel are required. Higher background illumination is usually required to observe the target with intensive light-emitting (e.g., the electric arc) or the Schlieren systems with a large FOV. However, the aperture of the collimating and converging lens in Toepler's lens-type Schlieren (or mirrors in Z-type) systems is usually in a range of $f/8$ to $f/12$, resulting in the fact that only a small amount of light from the point light source can be coupled to the Schlieren optics. A monochromatic high-power spotlight source, for example, laser light source or light-emitting diode (LED), is preferable to increase the intensity of the background illumination. However, as a coherent light source, the laser light source produces speckled patterns in the Schlieren image. Some techniques, for example, lens vibration or rotation, could be applied to reduce speckles, thus improving the image quality [54]. Such methods can only work under a frame rate of several hundreds of frames per second (fps). Achieving intensive background illumination under a frame rate of over tens of thousands of fps is still challenging. One feasible way is to operate the high-power LED at a short pulse mode, increasing the output power several times more than the LED operated at a continuous mode [55, 56]. We have tried several LED chips and found that Luminus PT-120G high-power LED module, with 4.6×2.6 mm emitting area, 5200 lm peak luminous flux, and 525 nm dominant wavelength, meets our requirements under most cases. Although modern monochrome complementary metal-oxide-semiconductor image sensors tend to achieve higher sensitivity at a wavelength longer than 700 nm [57], the red LED is not recommended for its much lower luminous flux than the green type.

TABLE 1 Comparison of four Schlieren optics systems

| | Toepler's lens-type | Z-type | Retro-reflective type | BOS type |
|--------------------|----------------------|-----------|-----------------------|----------|
| FOV | <15 cm | <50 cm | >1 m | >1m |
| Spatial resolution | High | High | Moderate | Low |
| Arrangement | Relatively difficult | Difficult | Easy | Easy |
| Cost | High | Moderate | Low | Low |

3.2 | Design the imaging system

When coupled with digital high-speed video cameras, as the read-out speed of the imaging sensor is limited, a high temporal resolution is obtained at the sacrifice of the FOV. For instance, the Photron SA-X2 camera can achieve a frame rate of 12,500 fps at 1024×1024 pixels, while only 128×48 pixels can be used if operated at a frame rate of 200,000 fps [57, 58]. In our experiments, although the Schlieren optics has the largest FOV of 20 cm, only a small region can be captured due to the instinctive limitation between the high-speed video camera's image size and frame rate. Considering the randomness of the discharge channel's propagation, the FOV of several centimetres is adjusted to cover the small region near the HV electrode from where the discharge always initiates.

The telephoto lens coupled with the camera is indispensable for the imaging system. The longer the lens's focal length, the narrower its angle of view and the higher the spatial resolution. Contrary to our intuition, an expensive and bulky telescope lens does not guarantee a higher level of details and higher image quality in a Schlieren system for two reasons. First, the aperture of the Schlieren optics is limited by the converging lens that cannot be wider than $f/8$, which means that an expensive bright lens with an $f/2.8$ or $f/4$ aperture cannot capture more light than a cheap lens with an F8 aperture. Second, the pixel density of the high-speed video camera is much lower than that in the commercial digital single-lens reflex (DSLR) camera, for which those telephotos are originally used. Moreover, the high-speed video camera is monochrome, so it is immune to the dispersion that can be inevitable in low-end lenses. Therefore, an entry-level telephoto lens with a moderate resolution and an aperture wider than $f/8$ can produce satisfactory Schlieren images.

4 | SCHLIEREN OBSERVATIONS FOR LONG SPARKS

Compared with the direct imaging techniques, the Schlieren techniques present the following advantages for long spark observations. (A1) It can eliminate the influence of discharge self-luminescence. (A2) It can locate the discharge channel by imaging the area with gas density changes, even if the discharge channel does not emit light or emits weakly. (A3) It is easy to achieve a spatial resolution of several hundred micrometres per pixel. (A4) It can quantitatively measure the gas density or temperature of the discharge channel based on some assumptions, which will be discussed in section 4.5. These

TABLE 2 Applications of the Schlieren technique in long spark observations

| No. | Long spark characteristics | Corresponding advantages |
|-----|-------------------------------------|--------------------------|
| 1 | Stem distribution | A1, A3 |
| 2 | Stem evolution during dark periods | A2, A3 |
| 3 | Stem elongation and branching | A1, A3 |
| 4 | Space stems | A1, A3 |
| 5 | Temperature of discharge channels | A4 |
| 6 | Shockwave visualisation | A1 |
| 7 | Decayed process for post-discharges | A2 |

advantages of Schlieren techniques can be used to obtain results that cannot be obtained by the direct imaging techniques when observing different processes of long sparks. Table 2 summarises applications of the Schlieren technique in observations of long spark characteristics and its corresponding advantages of the Schlieren technique.

4.1 | Stem distribution after the first streamer burst

The stem for the first streamer-corona burst typically has a diameter of 0.8–2 mm and a temperature range of 300–1500 K [11]. The stem is covered by a considerable amount of the luminosity of streamers [59], resulting in difficulties in measuring its geometric parameters. To observe such a tiny and non-thermal plasma channel, high sensitivity and high spatial resolution are required for the Schlieren photography. In these experiments [21, 60], the collimating and converging lenses were with a focal length of 200 cm. The high-speed video camera was operated at 200,000 fps, cooperated with a telephoto lens using the focal length of 500 mm. The temporal and spatial resolutions were $5 \mu\text{s}$ and $70 \mu\text{m}/\text{pixel}$, respectively. Accordingly, the FOV of the Schlieren system was 10.6×17.9 mm. Positive switching and lightning voltage impulses were applied to the HV electrode with different crest values and front times. Three electrodes with a radius of curvature of 0.1, 1, and 2 mm were used.

Figure 5 shows typical experimental results under the lightning and switching impulses. According to the Schlieren image in Figure 5b, several stems can be distinguished around the high-voltage electrode. In comparison, in the Schlieren image in Figure 5b, only one stem marked with a yellow arrow originates from the HV electrode tip. A large number of

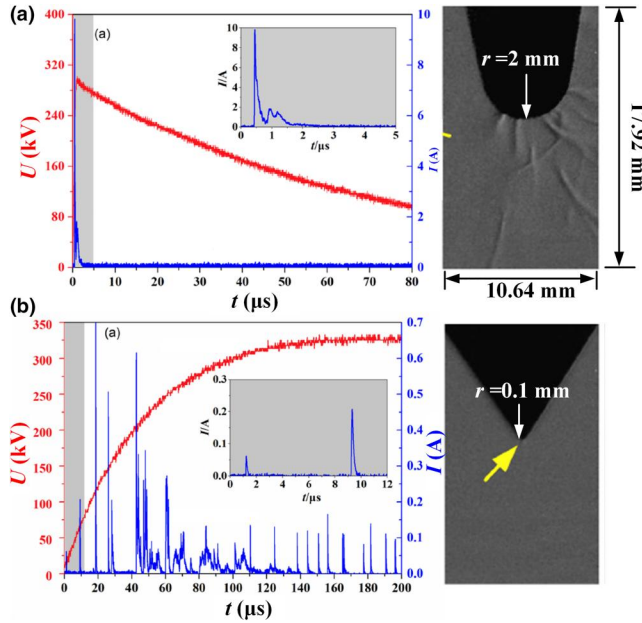


FIGURE 5 Synchronously recorded voltage impulse, current waveform, and corresponding Schlieren image under (a) lightning impulse applied to an electrode with a curvature radius of 2 mm and (b) switching impulse applied to an electrode with a curvature radius of 0.1 mm. [60]

experiments show that the front time of the applied voltage and the curvature radius of the high-voltage electrode have a great effect on the number and the distribution of stems after the first streamer burst [60, 61]. It is also found that the emergence of only one stem is preferable to the conditions with a slower change rate of the applied impulse and the electrode with a smaller curvature radius [60].

4.2 | Stem evolution during dark periods

After the first streamer-corona burst, the discharge channel may experience a dark period during which the electric current vanishes and the light-emitting stops. Optical cameras cannot observe such lightless processes, and the Schlieren technique can serve as a powerful tool instead [62–64]. Domens [65] compared two types of relaxation phases of the discharge channel with the first type in the vicinity of the anode and the second type further into the gap. The first type was found to have much more cooling efficiency than the second type. Due to the limited spatial resolution and image quality, the detailed evolution process of the decayed channel was not obtained.

To observe the refined process of channel evolution around the electrode, the Schlieren optics described in Section 4.1 was applied in the experiments [20]. Positive switching and lightning impulses were applied to the electrode with a radius of curvature of 0.1 mm, which was placed 0.74 m above the ground electrode.

Typical experimental results, including the synchronously recorded voltage and current waveforms and high-speed Schlieren frames, are presented in Figure 6. During the dark period, the front region of the channel tends to expand along

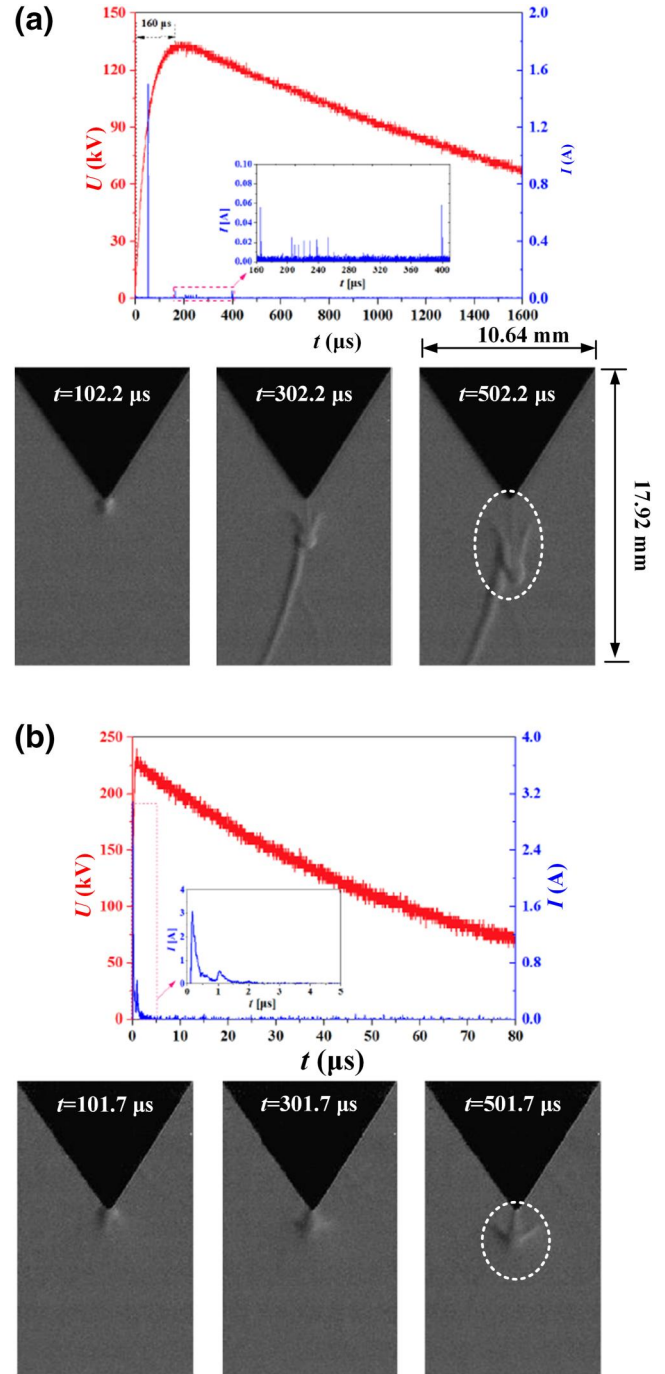


FIGURE 6 Typical results under (a) switching impulse with 135 kV crest value and 150 μ s front time as well as (b) lightning impulse with 230 kV crest value and 1.2 μ s front time. The synchronously recorded Schlieren images in each case are presented on the right side with a time interval of 200 μ s and an exposure time of 4 μ s. The mushroom-like structures are indicated with white circles. [20]

the radial direction while moving forward, changing its shape from a cylinder-shaped one to an arrow-shaped one in two dimensions. According to the law of the two-dimensional projection of a three-dimensional structure in Schlieren imaging in Figure 7 [66], the discharge channel in dark periods evolves similarly to the growth process of mushrooms as shown in Figure 8. It is the first time recognising the

mushroom-shaped structure around the electrode tip, which is important for further study on the re-illumination phenomenon in long sparks [67].

A simplified model, which considers the convection of natural gas, drift of ions subject to the time-varying electric field, and heat conduction of the electrode, has been proposed in [20] to simulate the channel evolution around the electrode tip. It is believed that the shock wave produced by the first streamer-corona burst is the main contributor to the formation of the mushroom-shaped structure, while the thermal conductivity of the electrode has a minor contribution.

4.3 | Stem elongation and branching

Recent high-speed optical images with exposure time lower than $2 \mu\text{s}$ have clearly shown that the streamers ahead of the leader channel have fine filamentary structures [68], challenging the idea that the streamer filaments converge into the bright zone, which were observed in earlier studies with optical photography techniques [59]. The morphology and the evolution of the stem may play an important role in the leader propagation and bifurcation. However, to the best of our knowledge, the measurement of the elongation and branching of stems along the discharge axis has not been reported.

In these experiments [69], another high-speed video camera (Phantom V1212) coupled with a Nikon 50 mm F1.2 lens was set up to capture the optical images with an interval of $5 \mu\text{s}$. Note that the exposure operations of two high-speed

cameras in the optical and Schlieren system were not strictly synchronized. Therefore, an error of several microseconds may exist in the exposure moment of these two cameras.

As shown in Figure 9b, the stem length and charge transfer in the second steamer burst vary from 3.53 to 7.35 mm and from 0.02 to 0.10 μC , respectively. This result challenges the previous assumption that the stem length produced by positive streamers remains constant. The relationship between the stem length L_{2s} and charge transfer Q_2 can be best-fitted by a power-law function as:

$$L_{2s} = 19 \times Q_2^{0.43} \quad (1)$$

where the L_{2s} and Q_2 are in the unit of mm and μC , respectively.

Figure 10 shows optical and Schlieren images, current waveforms of an event in which two additional streamers are produced after the second streamer burst with one of them developing into a leader channel. In this case, the second streamer leaves a track of low relative density. After a dark period of about $20 \mu\text{s}$, with the third streamer bursting, the root of the third discharge develops and defines a narrower streamer morphology along with the extension of the stem produced by the second burst as observed in Figure 10a. The streamer branches into a large number of filament ensembles after the fourth burst. Multiple pulses with an interval time of less than $1 \mu\text{s}$ can be distinguished in the corresponding current waveform. The above evidence supports that the streamer stems, produced by streamer branches, are important for the

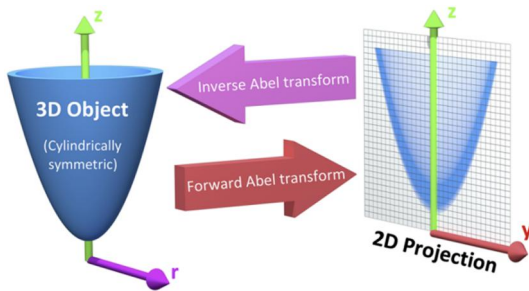


FIGURE 7 Illustration of the two-dimensional projection of the three-dimensional structure in Schlieren imaging. [82]

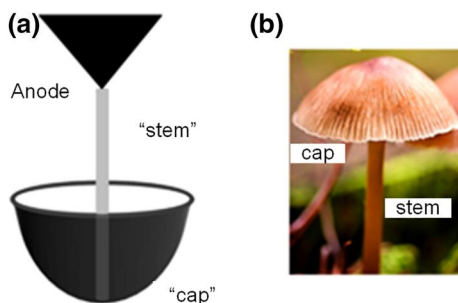


FIGURE 8 Illustration of the 3D structure of the discharge channel around the electrode tip during dark periods (a), which is analogous to a natural mushroom (b). [20]

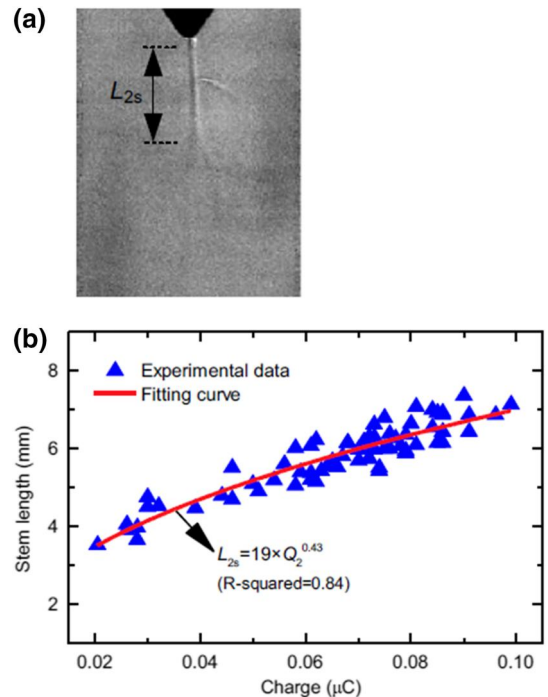


FIGURE 9 Stem elongation after the second streamer burst. A typical Schlieren image is shown in (a) with the parameter definition illustrated. The statistical results of the charge transfer in the second streamer versus the stem length are plotted in (b). [69]

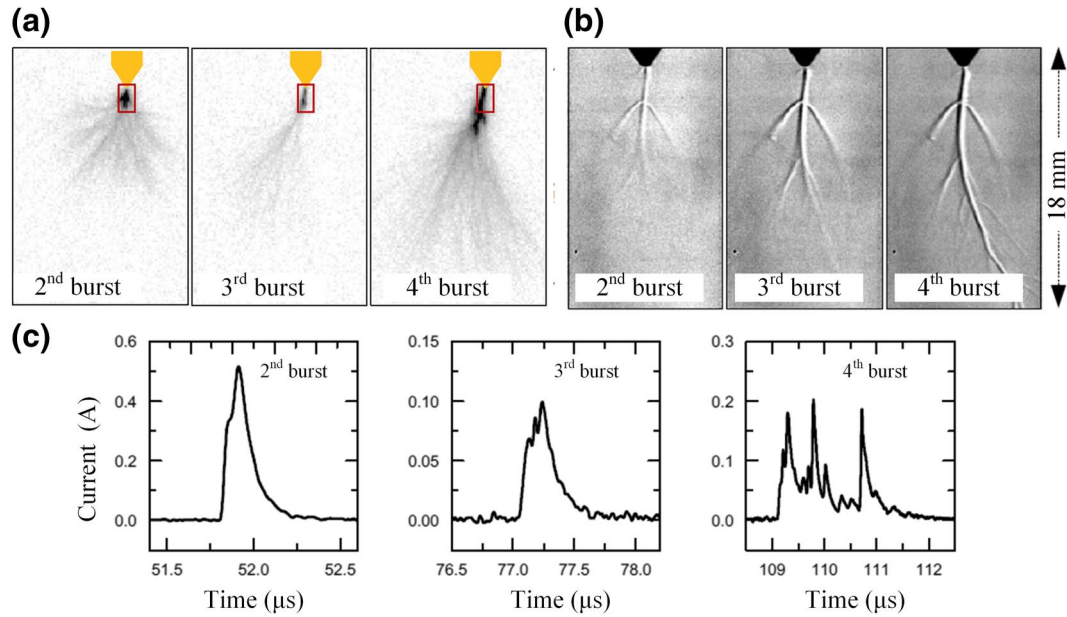


FIGURE 10 Elongation and branching of the stem in the second, third and fourth streamer burst with the high-speed optical and Schlieren image sequences shown in (a) and (b), respectively. The FOV of the Schlieren optics is indicated with red rectangles in the corresponding optical images. Associated electric current pulses are plotted in (c). [69]

inception of the leader channel and affect the propagation and branching of leader discharges [69].

4.4 | Suspended positive space stems

It is now commonly believed that the propagation of the negative leaders in long sparks is in stepped manners with the step formation process involving a space stem. In contrast, positive leaders under most common laboratory conditions tend to propagate continuously. However, some evidence of space leader ahead of the positive leader channel tip is reported by Kostinskiy, in which a framing ICCD camera was used [68]. As a new attempt, the high-speed Schlieren photography was applied to observe positive and negative leaders' stepped manner in our experiments.

Voltage impulses with different front times were applied. It was found that the stepped manners tend to occur under impulse voltage with a steep front. Accordingly, the following observation results are obtained under the positive and negative 1.2/50 μ s lightning voltage impulse. The high-speed video camera was operated at a frame rate of 200,000 fps and an exposure time of 3.3 μ s. The telephoto lens was fixed to 150 mm, achieving a spatial resolution of 280 μ m/pixel and an FOV of 4.2×7.1 cm. The relatively larger FOV increases the possibility of capturing the space stem in front of the HV electrode.

Typical Schlieren images in Figure 11 present a suspected positive space stem under the positive lightning impulse with a crest value of 400 kV and a space stem under the negative lightning impulse with the same amplitude. As shown in Figure 12a, the space stem under the positive impulse has a narrow head and a brush-like tail corresponding to the negative and positive

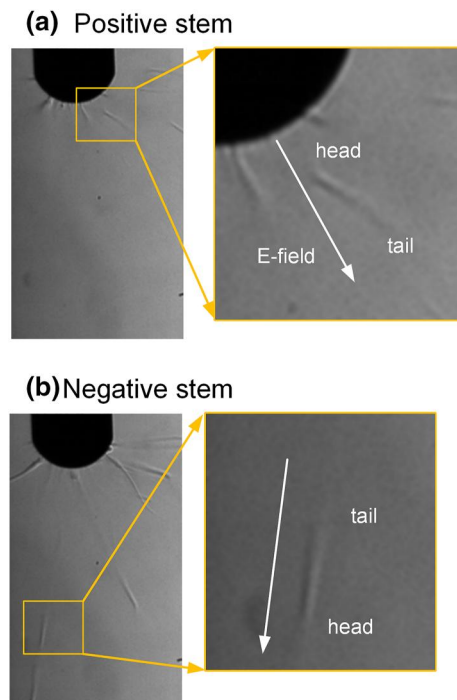


FIGURE 11 Suspected positive space stem and negative space stem under lightning impulse shown in (a) and (b). The direction of the electric field activated by the applied impulse is indicated with white arrows

streamers, respectively. The brush-like structure indicates that the positive streamer region involves more streamer filaments. However, the electric field at the trail is weaker than that in the head region because the latter is closer to the HV electrode. This can be explained that positive streamers initiate more easily, so

they can launch at a lower driving electric field [70, 71]. A similar structure is observed under negative lightning impulses with a typical Schlieren image shown in Figure 12b. The space stem under negative impulse has a symmetrical shape with the suspected space stem under positive impulse. Such symmetry of the stem under impulses with opposite polarities makes it possible that the positive space stem could also exist.

The distance between the suspected positive space stem and the electrode is measured with the results shown in Figure 12. The distance d is defined as the minimum distance between the space stem and the HV electrode or the leader channel if it exists. The average distance is about 8.7 and 23.9 mm under positive and negative impulse voltages, respectively. To a certain extent, these observations support the hypothesis proposed by Luque [72] that the positive space stem should have a shorter distance from the main channel than the negative one.

4.5 | Temperature profiles of discharge channels

With the continuous electric current flowing through the stem, the neutral gas inside the stem is heated until it reaches a temperature up to 2000 K [17, 73]. The “streamer-to-leader transition” is triggered at such a temperature, and the streamer stem is transformed to a thermalised leader segment [8]. The new segment merges into the leader body with the temperature increasing to 3000–5000 K [6, 11]. As the temperature plays an important role in this process, a direct measurement of the gas temperature profiles is of great help in understanding the mechanism of the transition process. To achieve this goal, the quantitative Schlieren techniques [74] are good choices.

To calibrate the Schlieren system, a quantitative relationship between the greyscale variation in Schlieren images and the reflection angle of the light beam has to be determined in the undisturbed case [64]. The reflection angle $\Delta\alpha$ in the undisturbed case can be equalised by the position deviation Δd of

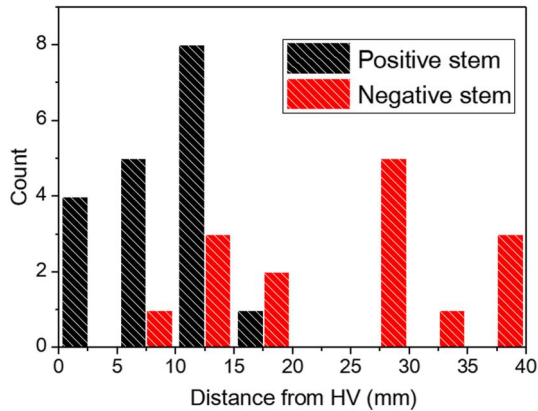


FIGURE 12 Statistical results of the distance between the suspected space stem and the electrode or main channel. The definitions of the distance are illustrated in corresponding figures

the knife edge. The knife edge is moved to cut different parts of the light source spot image, and the corresponding image greyscales are recorded. The linear relationship Δd and ΔG can be expressed as

$$\Delta G = m \cdot \Delta d = m \cdot f \cdot \Delta\alpha \quad (2)$$

where m is the slope of the so-called calibration curve shown in Figure 13. Another calibration method is placing a weak positive lens in the FOV. A light beam that passes through the lens will be refracted from a small angle. A similar equation as Eq. (2) can also be obtained.

The density distribution inside a thermalised leader channel could be assumed to be axisymmetric. Moreover, compared with the radial temperature gradient, the axial temperature deviation is much smaller. Therefore, the relationship between the reflection angle and the air density distribution can be built:

$$\Delta\alpha = \frac{2}{n_0} \int_0^\infty \frac{dn(r) \cdot r}{\sqrt{r^2 - x^2}} dr \quad (3)$$

where $n(r)$ is the air refractive index along the radial direction with the ambient value n_0 in the undisturbed region, x presents the coordinate axis parallel to the light beam with its origin located at $r = 0$.

By combining the equations (2) and (3), the air density at the specific point inside the discharge channel can be calculated from the greyscale deviation of the corresponding pixel in the Schlieren image. According to the simulation study, the discharge channel reaches a pressure equalisation within a time scale of less than 1 μ s. After that, the heating process in the discharge channel is isobaric [11, 17]. Therefore, the temperature distribution $T(r)$ can be calculated according to the ideal gas law:

$$T(r) = \frac{n(r)}{n_0} T_0 \quad (4)$$

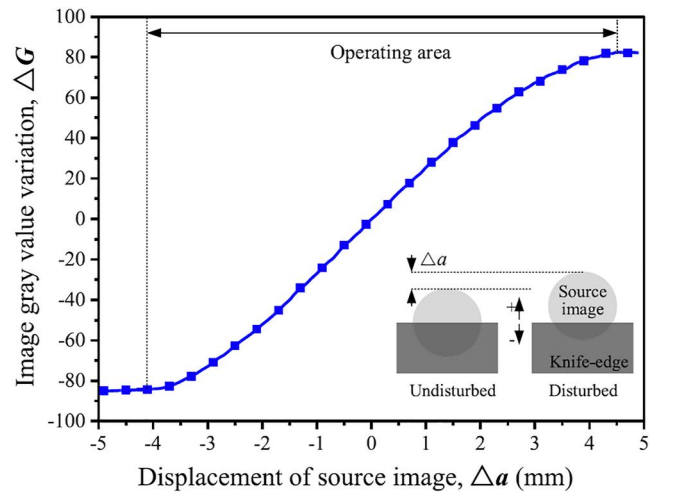


FIGURE 13 The calibration curve of the Schlieren system in the experiment [75]

where T_0 is the ambient temperature.

In this experiment [75], the positive impulse with a front time of $58 \mu\text{s}$ was applied to the HV electrode. As shown in Figure 14, after the first streamer-corona burst and a short dark period, the stem transforms to a leader channel and propagates towards the grounded plane with continuous electric current injected into the channel and ends up with a breakdown.

Figures 14c and 14d show the measured and simulated temperature and channel radius as a function of time at the axis of the leader channel. As the measurements show, the initial radius of the leader channel during the leader inception stage ranges between 0.1 and 0.3 mm, in good agreement with the simulation results. With the current being injected into the channel, the temperature rises from room temperature (300K) to over 3000 K. Due to the limited temporal and spatial resolutions, the measured temperature and the simulated results [17] are different at specific moments, while they are in good agreement in trend.

Using a telephoto lens with a focal length of 600 mm, Cheng [23] improved the spatial resolution to $48.5 \mu\text{m}/\text{pixel}$ and provided the temperature measurement results in a with-stand case with typical results shown in Figure 15.

As shown in Figure 15, the temperature first rises sharply to over 1000 K after the first streamer burst and roughly maintained during the first dark period. With the electric current associated with the second streamer burst, the channel is further heated to over 8000 K and dropped dramatically during the second dark period due to the heat convection. This result is in good agreement with the state-of-the-art simulation model [11] either in trend or at some specific moments.

4.6 | Shockwave visualisation

When the leader channel from the electrode finally reaches the grounded plane, a thin channel with high conductivity bridging the electrode and ground is formed. The electric current with an amplitude of several hundreds of amperes flows through the channel and heats the neutral air to over 10,000 K within a time scale of $1 \mu\text{s}$ [17]. High pressure is produced around the channel due to the fast heating process, resulting in the shock wave along the channel propagating in the normal direction [59, 73]. The high-speed Schlieren photography is a great candidate to visualise the shock front, where the air density varies. The high-speed video camera (Phantom V12.1) in the Schlieren system was operated at a frame interval of $7.7 \mu\text{s}$ and an exposure time of $1 \mu\text{s}$. In this way, the FOV reached $4.72 \times 2.37 \text{ cm}$ with a spatial resolution of $185 \mu\text{m}/\text{pixel}$. The light-emitting from the conductive channel itself is much more intensive than the background light source, so the channel parameter measurement is impractical under such an occasion. Instead of measuring the temperature directly, we used high-speed Schlieren images to analyse the shock waves accompanying the breakdown phase [32].

Figure 16 shows three different types of shock waves observed in the Schlieren images under either negative or positive voltage impulse. The first type is cylindrical shock wave (CSW) as shown in Figure 16a. The CSW occurs along the main channel, where the electric current passes through with a speed of 10^8 m/s . The CSW can be formed both along the straight and bending discharge channels. The second type is

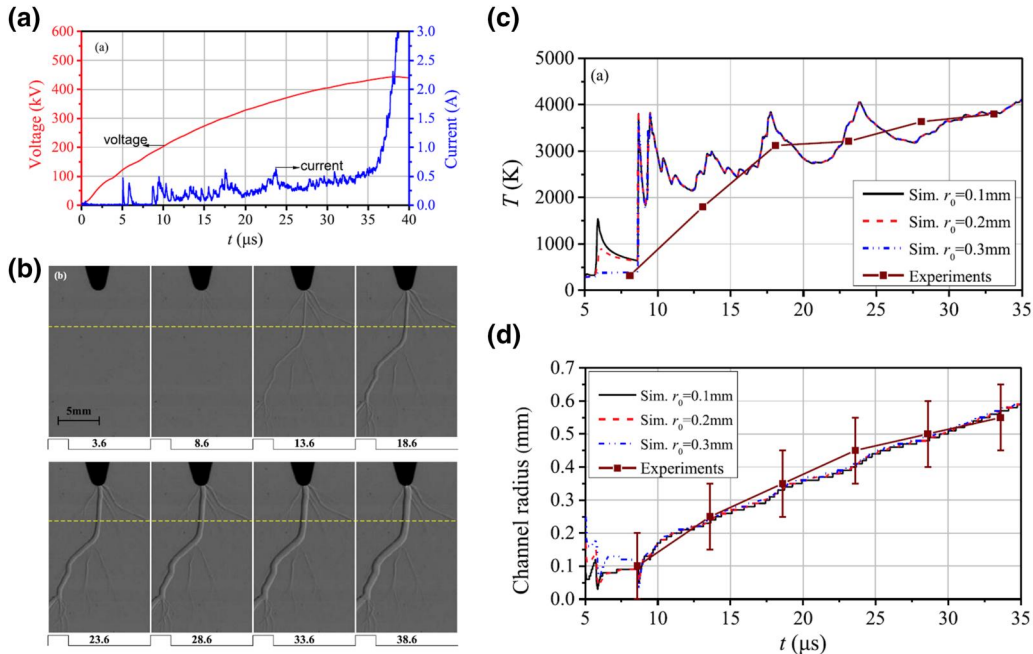


FIGURE 14 Experimental results for a breakdown case in a 1 m air gap under positive impulse with a crest value of 450 kV and a front time of $58 \mu\text{s}$: (a) waveforms of the applied voltage and associated electric current, (b) Schlieren image sequences with a frame interval of $5 \mu\text{s}$ and an exposure time of $1 \mu\text{s}$, (c) the temperature at the axis of the leader channel and (d) the thermal diameter. The cross-section in (b) is chosen to calculate the temperature is marked with a yellow-dotted line in image sequences. [75]

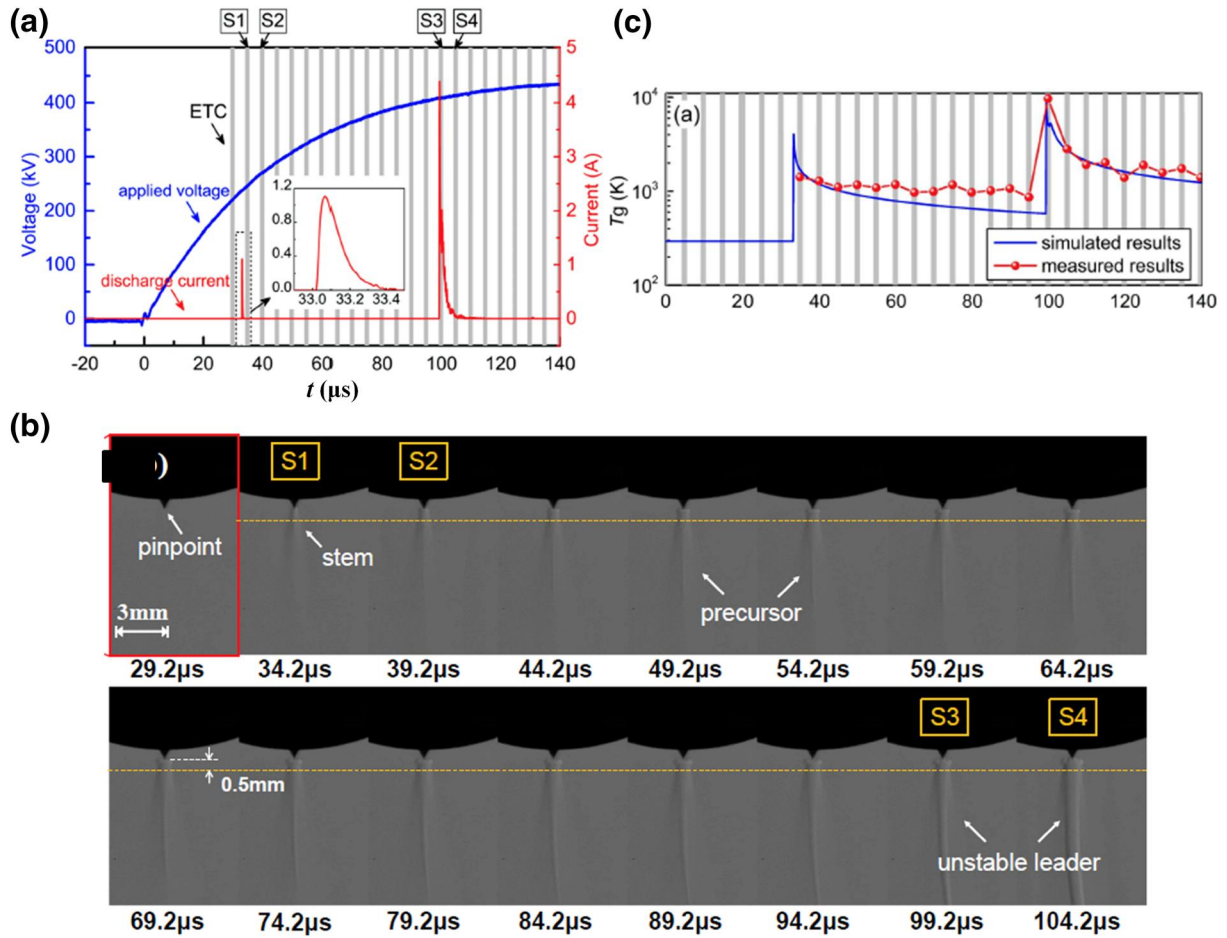


FIGURE 15 Experimental results for a withstand case in a 1 m air gap under positive impulse with a front time of 200 μ s. (a) Waveforms of the applied voltage and associated electric current, (b) Schlieren image sequences with a frame interval of 5 μ s and an exposure time of 1.25 μ s, and (c) calculated and simulated temperature at the axis of the leader channel varying with time. [23]

bow shock wave shown in Figure 16b, only appearing along the branching channel when the air gap is breakdown in our experiments. The uneven deposition of limited energy into the branching channel may contribute to forming this type of shock wave. The third type is spherical shock wave (SSW), observed at the connecting point between the space leader and the main leader, as shown in Figure 16c. Also, the SSW always occurs near the electrode as shown in Figure 16a and 16b. This may be due to the finite length domain where pressure increase can no longer be prolonged.

4.7 | Decayed process for post-discharges

After the breakdown, the electric current vanishes, and the channel temperature decreases [17]. The thermal convection process dominates in the post-discharge channel with a time scale that may reach several hundreds of milliseconds. Some researchers have observed the channel decay process in a short air gap under impulse or direct-current voltage impulses [34, 35]. However, observations of the evolution of discharge channels in long air gaps are still limited.

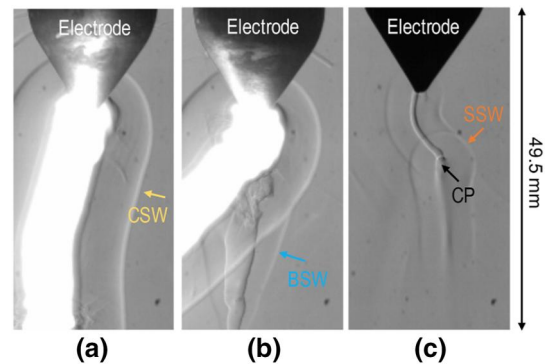


FIGURE 16 Three distinct shock wave types observed in Schlieren images: (a) the cylindrical shock wave (CSW), (b) the bow shock wave (BSW), and (c) the spherical shock wave (SSW). The CP in (c) indicates the connecting point of the negative leader and the space leader under the negative voltage impulse. [32]

The post-discharge evolution is much slower than the leader propagation phase. Therefore, the high-speed camera can be operated at a much slower speed to record the Schlieren images. In this way, the FOV can be a circle with a diameter of

15 cm with which the post-discharge channel evolutions were recorded in a 10-cm air gap.

The neural air is heated with a clear propagating shock wave with the electric current over 400 A flowing through the channel. As shown in the No.3 image in Figure 17b, when the low air density and high-temperature channel interact with the cool ambient air, the so-called Rayleigh-Taylor instability is triggered, and the edge of the channel becomes uneven [76]. According to No.5 image in Figure 17b, the uneven portion along the channel edge evolves to jet and propagates downward subsequently.

5 | SUMMARY AND OUTLOOK

The conventional Schlieren techniques offer new vistas in the long spark observations with the digital high-speed imaging system combination. The important features of high spatial resolution, high sensitivity, easy arrangement make the Schlieren techniques powerful tools for observing the discharge processes without light-emitting, for example, the stem evolution during the dark period and the insulation recovery process after the breakdown. Over the last decade, the high-speed Schlieren techniques, represented by the Toepler's lens-type optics, have been extensively used to observe the discharge process in the long air gap. Many interesting phenomena have been observed. Some of these discoveries provide a solid support for simulation models, while others deepen people's understanding of the physical mechanism behind the complicated discharge phenomena. The authors think that more interesting phenomena can be discovered with the Schlieren system further improved from the following aspects.

5.1 | Schlieren system with a higher spatial and temporal resolution

When the Schlieren optics are implemented with the still camera or the ultra-high-speed framing camera, the large FOV and high spatial resolution can be achieved simultaneously due

to the high pixel density of those cameras. For observing the slow process, for example, the channel decay process after breakdown, the still cameras represented by commercial DSLR (Digital-Single-Lens-Reflex Camera) can replace the high-speed video cameras. The typical DSLR has an image sensor of 24×36 mm with a pixel density of about $5 \mu\text{m}/\text{pixel}$ and a frame rate of 60 fps. The large sensor and high pixel density guarantee the large FOV and high spatial resolution. The frame interval of 16 ms is acceptable in the observation of the post-discharge process.

The ultra-high-speed framing ICCD camera is the only choice for observing the sub-microsecond process, for example, the streamer-to-leader process. The typical framing ICCD can achieve a pixel density of $5 \mu\text{m}/\text{pixel}$ and a frame interval of 1 ns. With the help of the image intensifier tubes, the framing ICCD camera can provide extremely high sensitivity and the exposure time as short as 1 ns. However, implementing a framing ICCD camera in a Schlieren system is not an easy task. First, the number of images obtained is usually limited, for example, 4–32 frames depending on different models. Therefore, a trigger signal must be fed to the camera before the streamer-leader-transition process that occurs randomly. A feasible method is to use the current signal to trigger the camera according to the findings of Huang [25] that the electric current flowing into the HV electrode increases a few microseconds before the streamer-leader-transition process during re-illumination phenomena. Another chokepoint of implementing the frame ICCD camera is that a slight difference exists on the frames from the same camera. Different frames are formed by different image intensifier and different image sensor units. Such differences cannot be negligible when the quantitative measurement is required.

5.2 | Imaging processing of Schlieren images

As analysed in Section 4.5, the Schlieren images can estimate the temperature profiles of the discharge channel under an

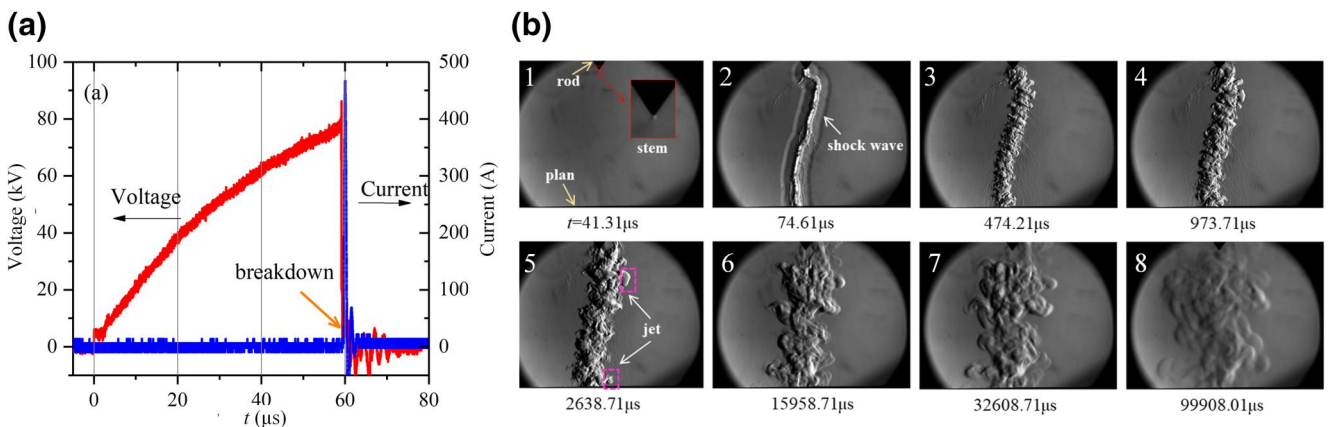


FIGURE 17 Experimental results in a 10 cm air gap under positive impulse with a crest value of 90 kV and a front time of $160 \mu\text{s}$: (a) waveforms of the applied voltage and associated electric current; (b) Schlieren image sequences with the exposure moments indicated in the corresponding images

axial symmetry assumption. An important factor that needs to be considered is the limited accuracy when measuring the temperature of thousands of Kelvins. Equation (3), which is used to calculate the air density, has a singularity at $r = 0$. Due to the high operation speed of the camera and spatial resolution limitation, the recorded Schlieren images are always noisy, which will cause huge errors when the Abel inversion algorithms are used directly to reconstruct the radial temperature of leader channels [77]. To solve this problem, the high-order total variation regularisation can be introduced in the Abel inversion to reduce the influence of image noise. The quantitative analysis from Liu [78] reveals that for a spatial resolution of $50 \mu\text{m}/\text{pixel}$, the error could be about 10% for temperature over 2000 K. The error can be reduced by improving the spatial resolution [79]. Therefore, a balance needs to be struck between the spatial resolution and FOV to achieve satisfactory accuracy for a specific observation target.

5.3 | Three-dimensional (3D) Schlieren

After the breakdown, the channel expanded randomly while exchanging heat with the surrounding air. Under this condition, the axial symmetry assumption of the channel no longer holds, making it impossible to calculate the density field from a single Schlieren image. To characterise the discharge channel's evolution in three dimensions, Schlieren images taken from different angles are required, bringing to life the 3D Schlieren techniques. Ishino [80] proposed a 3D-CT (Computer Tomography) system including 20-directional Toepler's lens-type Schlieren optics and cameras to reconstruct the 3D density field of the turbulent flames. Similar systems are constructed based on BOS optics and 23 industry cameras by Grauer [51]. In the impressive work of Liu [81], fibre bundles combine the Schlieren images from different directions together and feed the composite images to a high-speed camera, achieving 3D Schlieren imaging at a temporal resolution of 1 ms.

An FOV comparable with the air gap length is preferable to observe the insulation recovery process with full aspect. The retroreflective-type Schlieren, featuring with ease implementation and large FOV, serves as a good candidate in 3D Schlieren imaging of the metre-scale discharge channel. In the near future, we plan to build a 3D Schlieren imaging system based on a retroreflective screen to observe the post-discharge process.

ACKNOWLEDGEMENTS

This work was supported by the National Natural Science Foundation of China (51821005). X. Zhao would like to acknowledge the financial support of the China Postdoctoral Science Foundation (2018M633193).

DATA AVAILABILITY STATEMENT

The data that support the findings of this study are available from the corresponding author upon reasonable request.

ORCID

Xiankang Wang  <https://orcid.org/0000-0003-0260-8389>

Xianguan Zhao  <https://orcid.org/0000-0002-8476-2103>

REFERENCES

1. Bazelyan, E.M., Raker, Y.P.: *Lightning Physics and Lightning Protection*. CRC Press (2004)
2. Orville, R.E.: *Lightning Physics and Effects*. Cambridge University Press (2004)
3. Zeng, R., et al.: Survey of recent progress on lightning and lightning protection research. *High Volt.* 1(1), 2–10 (2016)
4. Liu, Z., et al.: Research on key technologies in ± 1100 kV ultra-high voltage DC transmission. *High Volt.* 3(4), 279–288 (2018)
5. Popov, N.A.: Investigation of the mechanism for rapid heating of nitrogen and air in gas discharges. *Plasma Phys. Rep.* 27(10), 886–896 (2001)
6. Popov, N.A.: Formation and development of a leader channel in air. *Plasma Phys. Rep.* 29(8), 695–708 (2003)
7. Popov, N.A.: Study of the formation and propagation of a leader channel in air. *Plasma Phys. Rep.* 35(9), 785–793 (2009)
8. Popov, N.A.: Fast gas heating in a nitrogen-oxygen discharge plasma: I. Kinetic mechanism. *J. Phys. D Appl. Phys.* 44(28), 285201 (2011)
9. Aleksandrov, N.L., Bazelyan, É.M., Konchakov, A.M.: Plasma parameters in the channel of a long leader in air. *Plasma Phys. Rep.* 27(10), 875–885 (2002)
10. Aleksandrov, N.L., et al.: A non-thermal mechanism of spark breakdown in Ar. *J. Phys. D Appl. Phys.* 32(20), 2636–2644 (1999)
11. Da Silva, C.L., Pasko, V.P.: Dynamics of streamer-to-leader transition at reduced air densities and its implications for propagation of lightning leaders and gigantic jets. *J. Geophys. Res. Atmos.* 118(24), 13561–13590 (2013)
12. Gallimberti, I.: The mechanism of the long spark formation. *J. Phys. Colloq.* 40(C7), 193–250 (1979)
13. Gallimberti, I., et al.: Fundamental processes in long air gap discharges. *Compt. Rendus Phys.* 3(10), 1335–1359 (2002)
14. Rizk, F.A.M., Vidal, F.: Modeling of positive leader speed under slow front voltages-Part I: long air gaps. *IEEE Trans. Power Deliv.* 23(1), 296–301 (2008)
15. Da Silva, C.L., Pasko, V.P.: Simulation of leader speeds at gigantic jet altitudes. *Geophys. Res. Lett.* 39(13), L13805 (2012)
16. Bazelyan, E., Raizer, Y.: *Spark Discharge*. CRC Press (1998)
17. Liu, L., Becerra, M.: Gas heating dynamics during leader inception in long air gaps at atmospheric pressure. *J. Phys. D Appl. Phys.* 50(34), 345202 (2017)
18. Xie, S., He, J., Chen, W.: An improved model to determine the inception of positive upward leader-streamer system considering the leader propagation during dark period. *Phys. Plasmas.* 20(4), 042107 (2013)
19. Xie, Y., et al.: The effect of corona discharge on leader initiation in long air gaps. *IEEE Trans. Plasma Sci.* 42(4), 890–895 (2014)
20. Zhao, X., et al.: Relaxation process of the discharge channel near the anode in long air gaps under positive impulse voltages. *J. Phys. D Appl. Phys.* 50(48), 485206 (2017)
21. Xiao, P., et al.: On the stem diameter under positive impulses in long air gaps. *Phys. Plasmas.* 26(6), 63501 (2019)
22. Zhou, X., et al.: A one-dimensional thermo-hydrodynamic model for upward leader inception considering gas dynamics and heat conduction. *Elec. Power Syst. Res.* 139, 16–21 (2016)
23. Cheng, C., et al.: Experimental study of the dynamics of leader initiation with a long dark period. *J. Phys. D Appl. Phys.* 53(20), 205203 (2020)
24. Zhao, X., et al.: Observations of the channel illuminations during dark periods in long positive sparks. *Geophys. Res. Lett.* 48(4), e2020GL091815 (2021)
25. Huang, S., et al.: The discharge preceding the intense reillumination in positive leader steps under the slow varying ambient electric field. *Geophys. Res. Lett.* 47(3), e2019GL086183 (2020)
26. Zhao, X., et al.: On the velocity-current relation of positive leader discharges. *Geophys. Res. Lett.* 46(1), 512–518 (2019)

27. Wang, Z., et al.: High-speed video observation of stepwise propagation of a natural upward positive leader. *J. Geophys. Res.* 121, 14.307–14.315 (2016)
28. Wang, X., et al.: A comparative study on the discontinuous luminosities of two upward lightning leaders with opposite polarities. *J. Geophys. Res. Atmos.* 125(12), e2020JD032533 (2020)
29. Wu, T., Wang, D., Takagi, N.: Velocities of positive leaders in intracloud and negative cloud-to-ground lightning flashes. *J. Geophys. Res. Atmos.* 124(17–18), 9983–9995 (2019)
30. Gürlek, A.: Breakdown process on rod–rod air gap under oscillating lightning impulse voltage. *High Volt.* 5(3), 319–326 (2020)
31. Aleksandrov, N.L., Bazelyan, E.M.: Ionization processes in spark discharge plasmas. *Plasma Sources Sci. Technol.* 8(2), 285–294 (1999)
32. Liao, Y., et al.: Shock wave propagation in long laboratory sparks under negative switching impulses. *J. Phys. D Appl. Phys.* 54(1), 015205 (2020)
33. Shurupov, M.A., et al.: Gasdynamic instabilities during decay of the sub-microsecond spark discharge channel. *High Temp.* 52(2), 169–178 (2014)
34. Greig, J.R., Pechacek, R.E., Raleigh, M.: Channel cooling by turbulent convective mixing. *Phys. Fluids.* 28(8), 2357–2364 (1985)
35. Leonov, S.B., et al.: Jet regime of the afterspark channel decay. *Phys. Plasmas.* 17(5), 53505 (2010)
36. Group, L.R.: Research on long air gap discharges at les Renardières–1973 results. *Electra.* 35, 49–156 (1974)
37. Yue, Y., et al.: Characteristics of long air gap discharge current subjected to switching impulse. *CSEE J. Power Energy Syst.* 1(3), 49–58 (2015)
38. Zhao, X., He, J., He, H.: Effect of branching on spikes of positive leader current. *IEEE Trans. Dielectr. Electr. Insul.* 23(4), 1968–1973 (2016)
39. Xie, Y., et al.: An experimental and numerical study of leader development in rod-rod gaps under positive switching impulse voltage. *EPJ Appl. Phys.* 64(1), 10802-p1–10802-p7 (2013)
40. Zeng, R., Chen, S.: The dynamic velocity of long positive streamers observed using a multi-frame ICCD camera in a 57 cm air gap. *J. Phys. D Appl. Phys.* 46(48), 485201 (2013)
41. Settles, G.S.: *Schlieren and Shadowgraph Techniques: Visualizing Phenomena in Transparent Media.* Springer Science & Business Media (2001)
42. Settles, G.S., Hargather, M.J.: A review of recent developments in schlieren and shadowgraph techniques. *Meas. Sci. Technol.* 28(4), 42001 (2017)
43. Hargather, M.J., Settles, G.S.: Retroreflective shadowgraph technique for large-scale flow visualization. *Appl. Opt.* 48(22), 4449–4457 (2009)
44. Talley, M.A., Jones, S.B., Goodman, W.L.: Development of a Large Field of View Shadowgraph System for a 16 Ft. Transonic Wind Tunnel' Citeseer (2000)
45. Raffel, M.: Background-oriented schlieren (BOS) techniques. *Exp. Fluid.* 56(3), 1–17 (2015)
46. Sutherland, B.R., et al.: Visualization and measurement of internal waves by synthetic schlieren. Part 1. Vertically oscillating cylinder. *J. Fluid Mech.* 390, 93–126 (1999)
47. Goldhahn, E., Seume, J.: The background oriented schlieren technique: sensitivity, accuracy, resolution and application to a three-dimensional density field. *Exp. Fluid.* 43(2), 241–249 (2007)
48. Meier, G.E.A.: Computerized background-oriented schlieren. *Exp. Fluid.* 33(1), 181–187 (2002)
49. Richard, H., Raffel, M.: Principle and applications of the background oriented schlieren (BOS) method. *Meas. Sci. Technol.* 12(9), 1576 (2001)
50. Goldhahn, E., et al.: Quantitative measurements of three-dimensional density fields using the background oriented schlieren technique. In: *Imaging Measurement Methods for Flow Analysis*, pp. 135–144. Springer (2009)
51. Grauer, S.J., et al.: Instantaneous 3D flame imaging by background-oriented schlieren tomography. *Combust. Flame.* 196, 284–299 (2018)
52. Sourgen, F., Leopold, F., Klatt, D.: Reconstruction of the density field using the colored background oriented schlieren technique (CBOS). *Opt. Laser. Eng.* 50(1), 29–38 (2012)
53. Kolhe, P.S., Agrawal, A.K.: Density measurements in a supersonic microjet using miniature rainbow schlieren deflectometry. *AIAA J.* 47(4), 830–838 (2009)
54. Tu, S.-Y., Lin, H.Y., Lee, T.-X.: Efficient speckle-suppressed white light source by micro-vibrated and color-mixing techniques for lighting applications. *Opt. Express.* 23(20), 26754–26768 (2015)
55. Willert, C., et al.: Pulsed operation of high-power light emitting diodes for imaging flow velocimetry. *Meas. Sci. Technol.* 21(7), 75402 (2010)
56. Willert, C.E., Mitchell, D.M., Soria, J.: An assessment of high-power light-emitting diodes for high frame rate schlieren imaging. *Exp. Fluid.* 53(2), 413–421 (2012)
57. Vision Research: Phantom Ultra High-Speed UHS-12 Camera Datasheet (2021)
58. Photron: FastCam SA-X2 Manual (2014)
59. Bazelyan, E.M., Raizer, Y.P., Aleksandrov, N.L.: The effect of reduced air density on streamer-to-leader transition and on properties of long positive leader. *J. Phys. D Appl. Phys.* 40(14), 4133–4144 (2007)
60. Yang, Y., et al.: Number of stems around the H.V. electrode in a 0.74-m air gap under positive impulse. *Phys. Plasmas.* 25(10), 103513 (2018)
61. Jiang, Z., et al.: Distribution of stems around the HV electrode in a 0.74-m air gap under positive pulses. *IEEE Trans. Dielectr. Electr. Insul.* 25(1), 372–375 (2018)
62. Domens, P., et al.: Large air-gap discharge and schlieren techniques. *J. Phys. D Appl. Phys.* 21(11), 1613–1623 (1988)
63. Xu, D.A., et al.: Thermal and hydrodynamic effects of nanosecond discharges in atmospheric pressure air. *J. Phys. D Appl. Phys.* 47(23), 235202 (2014)
64. Alvarez-Herrera, C., et al.: Temperature measurement of air convection using a schlieren system. *Opt. Laser. Technol.* 41(3), 233–240 (2009)
65. Domens, P., et al.: Leader filament study near the anode in a rod plane gap. *J. Phys. D Appl. Phys.* 24(7), 1088–1097 (1991)
66. Hargather, M.J., Settles, G.S.: A comparison of three quantitative schlieren techniques. *Opt. Laser. Eng.* 50(1), 8–17 (2012)
67. Zhao, X., et al.: Re-illumination of streamer stems under either rising or non-changing positive electric fields in long air gaps. *AIP Adv.* 11(5), 055303 (2021)
68. Kostinskiy, A.Y., et al.: Abrupt elongation (stepping) of negative and positive leaders culminating in an intense corona streamer burst: observations in long sparks and implications for lightning. *J. Geophys. Res. Atmos.* 123(10), 5360–5375 (2018)
69. Zhao, X., et al.: Elongation and branching of stem channels produced by positive streamers in long air gaps. *Sci. Rep.* 11(1), 1–11 (2021)
70. Liu, N., et al.: Formation of streamer discharges from an isolated ionization column at subbreakdown conditions. *Phys. Rev. Lett.* 109(2), 25002 (2012)
71. Dwyer, J.R., et al.: X-ray bursts associated with leader steps in cloud-to-ground lightning. *Geophys. Res. Lett.* 32(1), L01803 (2005)
72. Malagón-Romero, A., Luque, A.: Spontaneous emergence of space stems ahead of negative leaders in lightning and long sparks. *Geophys. Res. Lett.* 46(7), 4029–4038 (2019)
73. Liu, L., Becerra, M.: On the critical charge required for positive leader inception in long air gaps. *J. Phys. D Appl. Phys.* 51(3), 35202 (2018)
74. Tobin, J.D., Hargather, M.J.: Quantitative schlieren measurement of explosively-driven shock wave density, temperature, and pressure profiles. *Prop. Explos. Pyrotech.* 41(6), 1050–1059 (2016)
75. Zhao, X., et al.: On the use of quantitative Schlieren techniques in temperature measurement of leader discharge channels. *Plasma Sources Sci. Technol.* 28(7), 075012 (2019)
76. Sharp, D.H.: An Overview of Rayleigh-taylor instability. *Phys. D.* 12(1-3), 3–18 (1983)
77. Ma, S.: Tomography of cylindrical objects: comparison of noise property and accuracy of Abel inversion techniques with and without noise filtering. *Appl. Opt.* 50(35), 6512–6521 (2011)
78. Liu, X., et al.: An improved inversion algorithm to reconstruct 2D temperature fields of long sparks with high-speed schlieren technique. *Measurement.* 180, 109620 (2021)

79. Aleiferis, P., et al.: Schlieren-based temperature measurement inside the cylinder of an optical spark ignition and homogeneous charge compression ignition engine. *Appl. Opt.* 54(14), 4566–4579 (2015)
80. Ishino, Y., et al.: Schlieren 3D-CT reconstruction of instantaneous density distributions of spark-ignited flame kernels of fuel-rich propane-air premixture. In: *Heat Transfer Summer Conference*. American Society of Mechanical Engineers (2016).V001T06A005
81. Liu, H., Shui, C., Cai, W.: Time-resolved three-dimensional imaging of flame refractive index via endoscopic background-oriented Schlieren tomography using one single camera. *Aero. Sci. Technol.* 97, 105621 (2020)
82. Hickstein, D.D., et al.: A direct comparison of high-speed methods for the numerical Abel transform. *Rev. Sci. Instrum.* 90(6), 065115 (2019)

How to cite this article: He, J., et al.: Schlieren techniques for observations of long positive sparks: Review and application. *High Voltage*. 1–15 (2022). <https://doi.org/10.1049/hve2.12225>